

Systems and control challenges in photovoltaic manufacturing processes – A modeling strategy for passivation and anti-reflection films

Raymond A. Adomaitis* Alexander Schwarm**

* *Department of Chemical and Biomolecular Engineering, Institute for Systems Research, University of Maryland, College Park, MD 20742, USA (email: adomaiti@umd.edu)*

** *Automation Products, Applied Global Services, Applied Materials, Inc. (email: Alexander_Schwarm@amat.com)*

Abstract: A view of contemporary systems and control challenges in PV cell manufacturing is given in this paper, with emphasis on developing a modeling strategy for the optimization of thin-film silicon nitride $\text{SiN}_x\text{:H}$ films used for passivation and anti-reflection coatings in single (*sc*-) and multicrystalline silicon (*mc*-Si) solar cells. The overall framework integrates three modeling modules: a remote plasma-enhanced chemical vapor deposition (RPECVD) reactor *process model* that predicts film composition and thickness based on process input parameters, a *solar-optical module* that translates the film physical and chemical properties to PV cell photo-generated current, and a PV cell equivalent circuit *device model* that predicts cell power output and efficiency from the film properties and photocurrent. Because the model couples process inputs to both PV cell performance and manufacturing process efficiency, the modeling approach is ideal for optimizing process and product performance.

Keywords: photovoltaic solar cell; process simulation; process optimization; chemical vapor deposition.

1. INTRODUCTION

Integrated over the spectrum, the normal incident solar radiation on a clear day reaching the Earth's surface corresponds to a flux of 1 kW/m^2 . Despite the intense scientific and engineering efforts to improve solar cell design, current practical PV cells convert only a fraction of the solar flux to usable electrical power. A combination of factors contribute to the low efficiency of PV cells, such as the intrinsic semiconductor material properties (e.g., the band gap of each device layer), the device design (the number and type of junctions), and the quality of the device elements themselves (e.g., defects that result in recombination sites).

Microelectronics and PV device manufacturing processes share a number of common unit operations and manufacturing goals, so it is not unexpected that the latter has benefited from the large research investment made in process and manufacturing engineering of the former. However, because of the simplicity of PV relative to ULSI devices, the goal of modeling the entire PV manufacturing process, from substrate to final device efficiency, is in reach. In this paper we will examine the connection between one step in PV manufacturing and ultimate device performance. Our focus will be the deposition of silicon nitride anti-reflection (AR)/passivation coatings, a key process that has led to

the resurgence of domestic manufacturing of crystalline silicon (*mc*- and *sc*-Si) PV cells.

The objective of this paper is to develop the modeling strategy shown in Fig. 1; our complete model is comprised of three major components, with the goal of formally connecting manufacturing process inputs to device outputs to make sense of the sometimes conflicting observations made in the literature. The first is the physically based manufacturing *process model* describing the relationship between the manipulated variables (substrate temperature T , total pressure P , etc., to be described later) and the AR film characteristics, such as thickness and composition. The film characteristics become input to both the *solar-optical* and the *device models* to determine the total solar energy captured and then to assess cell I versus V characteristics and overall cell efficiency η . Ultimately, our goal is to use the complete model in conjunction with an optimization objective function based on maximizing tool productivity (throughput and precursor utilization) and PV cell efficiency.

1.1 Multicrystalline silicon substrates

PV cell design is generally split between thin-film (*a*-Si, CIGS, CdTe) and Si-substrate cells. Let us consider the entire manufacturing process for creating multicrystalline silicon (*mc*-Si) solar cells, starting with the production of the Si substrates that form the base of the PV cell

* RAA acknowledges the support of the National Science Foundation through grant NSF-CBET 0828410.

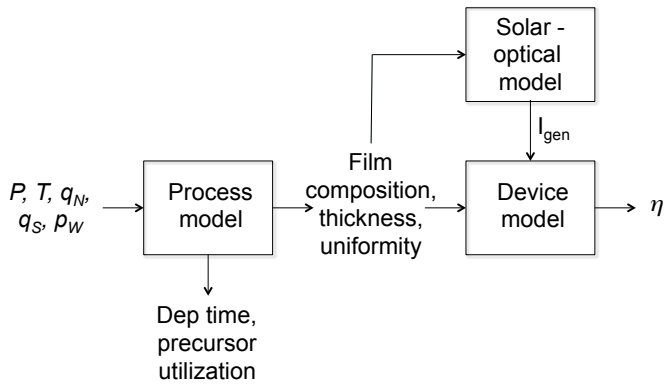


Fig. 1. The integrated PV cell process/device modeling strategy.

(additional details can be found in the overviews by Ceccaroli and Lohne (2003) and Ranjan et al. (2011)).

The first step of the process is SiO_2 reduction in which lumpy quartz is converted to metallurgical-grade Si. The primary reaction $\text{SiO}_2(\text{s}) + 2\text{C}(\text{s}) \rightarrow \text{Si}(\text{l}) + 2\text{CO}(\text{g})$ takes place in a carbon electrode arc furnace at approximately 2200 K. Additional reactions compete with the Si production in the furnace, such as those producing SiC.

Iron, boron, and aluminum remain as some of the impurities in the metallurgical-grade Si. Silicon hydrochlorination is the first step to removing these impurities. The reactions take place in a fluidized-bed reactor at approximately 300 °C, with the primary reaction $\text{Si} + 3\text{HCl} \rightarrow \text{H}_2 + \text{SiHCl}_3$. Other chlorosilanes (e.g. SiCl_4 , SiH_2Cl_2) are produced, as well as other chlorinated impurities. Fortunately, these compounds have widely varying boiling points, and so it is a simple matter to design two sequential distillation columns capable of producing a relatively pure product stream of SiHCl_3 .

As the final purification step, chemical vapor deposition (the Siemens CVD process) is used to produce electronic grade silicon (EGS) using the SiHCl_3 precursor. It is interesting to note that the CVD reaction is essentially the exothermic hydrochlorination reaction operated in reverse; the gas-phase equilibrium reaction $\text{SiHCl}_3(\text{g}) + \text{H}_2(\text{g}) \rightleftharpoons \text{Si}(\text{s}) + 3\text{HCl}(\text{g})$ is driven to the right by operating the CVD process at a high temperature (1400 K). 200-300 hours of deposition time are required to produce the solid, EG polycrystalline silicon.

Multicrystalline Si ingots then are created from a combination of polycrystalline Si and waste EGS from the semiconductor industry. Molten Si is pored into crucibles and solidification takes place from the bottom up. Small, mostly vertical crystals (grains) are formed during the solidification process; this directionality is important to the operation of the final solar cell. For *p*-type Si, a small amount of boron is added to the molten Si prior to pouring the mixture in the crucible. In the final wafering process, a wire saw is used to slice the Si ingots into $\approx 180 \mu\text{m}$ thick wafers. Many parallel cutting wires and an SiC cutting solution is used in the process, where the cuts are made perpendicular to the long crystal grains, resulting in the rectangular wafers distinctive to *mc*-Si cells. Kerf losses and surface roughness are important considerations in the wafering operation.

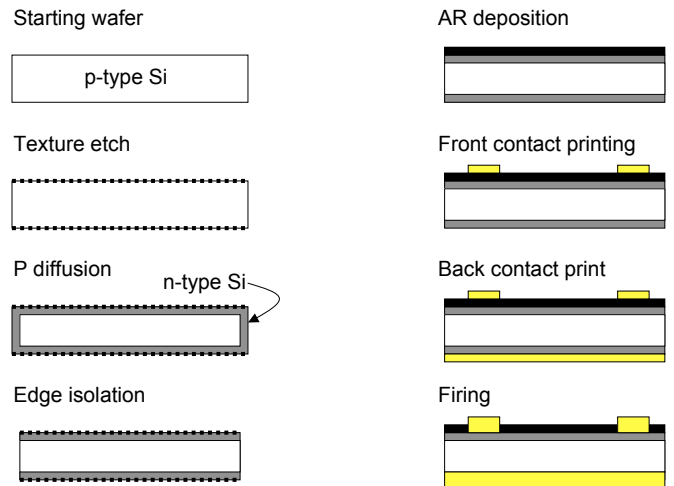


Fig. 2. Sequence of *mc*-Si solar cell fabrication steps.

1.2 PV cell fabrication processing steps

Starting with the *p*-doped Si wafer described, an overview of the basic steps relevant to *mc*-Si (and single crystal *sc*) PV cell manufacturing are shown in Fig. 2. We now consider each step in sequence.

Surface finishing/texturing Chemical etching is used to smooth wire-saw marks. Likewise, KOH or NaOH solutions can be used to texture the surface to decrease light reflection, whereby the μm -scale pyramidal surface features result in a higher probability that a reflected photon encounters another portion of the cell surface.

Phosphorous diffusion To create the semiconductor junction necessary for charge separation, a phosphorous precursor (e.g., gas P_2H_2 , liquid POCl_3 , or solid-source precursor P_2O_3) are used in a furnace operating at 1200 K to diffuse the P into the Si to form the an *n*-type layer surrounding the thicker, bulk *p*-type substrate.

Edge isolation The wafer edge doping is removed to prevent short circuits through the PV device, increasing the cell's shunt resistance.

AR deposition Reflectance loss for bare Si in air can be as high as 30%. Antireflection (AR) coatings reduce losses below 10%, and potentially to $< 1\%$ when combined with the texturing described earlier. AR coatings typically consist of CVD titanium dioxide or PECVD silicon nitride. The thickness of these coatings is set to the wavelength-dependent optimal value. Material refractive index is important and AR coating compositions are chosen to give a refractive index between the values of glass (or air) and silicon. Substantially more will be said later in this paper regarding this processing step.

Front contact printing A silver paste mixture in an organic binder is used in a screen-printing process to produce the front contacts. Line widths are $\approx 50 \mu\text{m}$ and the design of the contact pattern is nontrivial (Wenham et al. (2007)). Front contact shading can account for up to 10% loss of cell surface area.

Back contact The back contact is deposited as a metal paste containing silver and aluminum, the latter is needed to produce an ohmic contact with the p -type Si layer.

Firing With the front/back contacts applied, the final assembly is fired to remove the contact organic binders and to drive the Al contacts through the n -type back layer into the p -layer and the front contacts through the AR film. This thermal process also can profoundly affect other characteristics of the cell performance.

At this point the PV cell is operational. However, for a workable panel, the cells, typically producing 0.5 V and 3.6 A from each $10 \times 10 \text{ cm}^2$ cell, remain to be wired and packaged; these aspects of panel design are described by Wenham et al. (2007).

1.3 PV cell manufacturing challenges and opportunities for process systems engineering advances

Currently, the solar industry has entered a period in which rapid changes are occurring over a very short period of time. To put this in perspective, in the thirty-five years since the first crystalline silicon solar cell was developed, there have been five major technological development steps: 1) screen printing; 2) glass/EVA/TEDLAR; 3) wire saw 4) silicon nitride; and 5) metrology. Now, just in the past two years, we have witnessed the addition of five new advances: 1) double print; 2) selective emitter; 3) back passivation; 4) point contacts; and 5) optical and minority carrier mirrors. This rapid acceleration has been fueled by the approximately \$3 to \$5 billion per year spent and 70,000 researchers currently working on research and development (Gay (2011), C. Breyer et al. (2010)). One area gaining importance is the impact of passivation on cell efficiency for current and emerging cell designs, a processing topic we explore in detail later in this paper. We note that passivation is not just focused on the front side and associated surface recombination and antireflection, but on the backside of the cell as well.

The primary driving factor for decisions made by solar manufacturers is the simple equation of cost per Watt. The decision to choose to purchase new equipment for a process step to improve cell efficiency or yield ultimately will be decided by examining the efficiency or additional Watt peak output of the cell divided by the amortized cost of the equipment for each of the cell produced over the expected life of the equipment. Combining process and device models allows us to trade-off and optimize these two factors.

For silicon ingot formation a technique which is called “mono casting” is showing some promise. In this case, a monocrystalline ingot is cast (not pulled, such as in the Czochralski process). This is a much faster and therefore less expensive process. Typically portions of the ingot are still multicrystalline, but large sections are monocrystalline. Currently the split in manufacturing is 80% multi- and 20% monocrystalline. Better casting process control will improve monocrystalline yield and subsequently will have a significant influence on the industry. In a typical multicrystalline cell line 60-80% of the product quality variability is due to the incoming wafer quality. For a monocrystalline cell line, the incoming wafer quality ac-

counts for 20-40% of the product quality variability. If manufacturers find an inexpensive method of producing monocrystalline wafers to yield a 1% cell efficiency increase over multicrystalline based cells, a significant opportunity for process optimization and process control will be opened because the Pareto of variability will shift to the processes instead of the feedstock.

Another exciting opportunity is to take advantage of newer metrology techniques, such as photoluminescence, to measure incoming wafer quality. Although still under development, this information can be used to adapt processes to incoming material variations to perform so-called Material Adaptive Processing or MAPTM.

Finally, newer cell structures are gaining popularity with cell manufacturers. These can be characterized as relatively minor modifications to cell design and so the resulting manufacturing modifications are limited to a few processing steps. One example is the case of the double print process, which adds a second screen print step with specialized paste to increase the aspect ratio of the printed conductive lines without increasing resistance. Likewise are the selective emitter designs, where the addition of a deposition or implantation step provides a highly doped region under the conductive lines. The next set of advancements, including metal wrap-through, emitter wrap-through, and interdigitated back contact cell designs, constitute more significant changes in cell structure, changes that impact not only cell manufacturing but module manufacturing as well.

1.4 Amorphous $\text{SiN}_x\text{:H}$ structure and composition

This study focuses on the AR/passivation layer, how its properties depend on the deposition process conditions, and how the composition and thickness of the film affect the PV cell efficiency. Crystalline silicon nitride is written with the chemical formula Si_3N_4 ; because the anti-reflection/passivation films are deposited in amorphous form and contain a significant amount of hydrogen, the films are denoted as $\text{SiN}_x\text{:H}$ with $x = 1.33$ corresponding to a stoichiometric N/Si ratio. A depiction of the film molecular structure and typical film compositions are given in Fig. 3. These data are taken from Zerga et al. (2007) with limiting values denoted by *. We note that Alvarez and Valladares (2002) suggest N-N bonds do not exist in these films, a fact we use in Section 5.3 in developing rate expressions for the surface reactions.

A number of the film optical and electrical properties vary strongly with film composition. For example, the film refractive index n_1 has been shown to display the linear compositional dependence (proportional to Si/N) $n_1 = 0.7/x + 1.39$ by Masi et al. (1994) whereas the same functionality but different coefficient values $n_1 = 0.61/x + 1.22$ are reported by Lelievre et al. (2009). Therefore, for the purposes of this study we will take

$$n_1 = \frac{0.65}{x} + 1.3 \quad (1)$$

Significantly less information is available on measured film band gap $E_{bg,1}$ as a function of x ; Soppe et al. (2005) state the band gap decreases with increasing Si content from 5.3

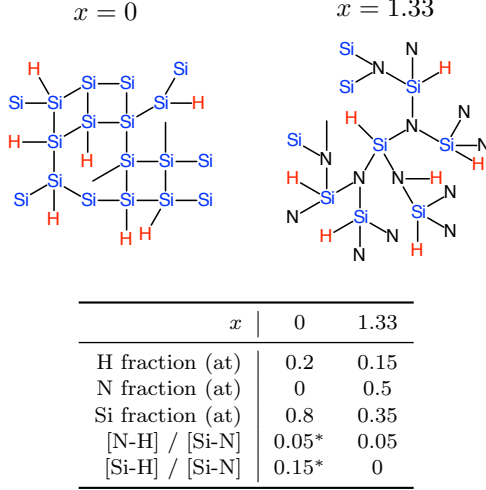


Fig. 3. Amorphous $\text{SiN}_x\text{:H}$ corresponding to a stoichiometric films (right) and the limiting case of a pure amorphous Si film (left); data are taken from Zerga et al. (2007).

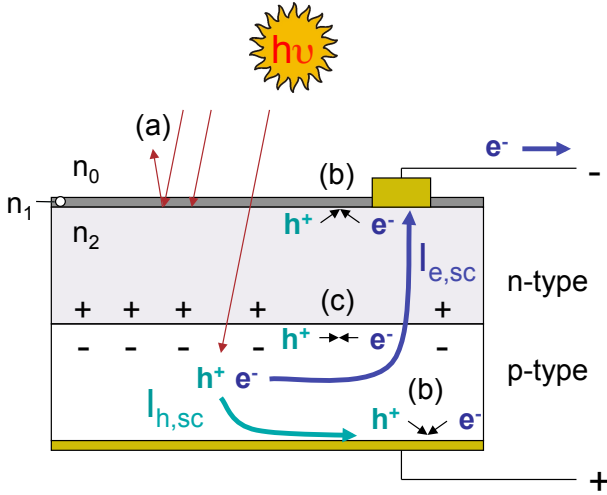


Fig. 4. The mc- or sc-Si solar cell. We note that the n-type layer normally forms the top (sun-facing) surface of a solar cell. The n-type top layer is the emitter (thickness $\approx 1 \mu\text{m}$), the bottom (substrate) is the base, with nominal thickness of $100 \mu\text{m}$.

eV for a stoichiometric film to 1.8 eV for amorphous Si. Assuming a linear relationship we find

$$E_{bg,1} = 1.8 + 2.63x \text{ eV}. \quad (2)$$

Finally, the density ρ is necessary to compute film growth rate in the deposition reactor model. A range of values have been reported, from Dollet et al. (1995) who give a film density value of $\rho = 2110 \text{ kg/m}^3$ for amorphous silicon nitride films to King (2011) who reports $\rho = 2700 \text{ kg/m}^3$. We will assume a value of $\rho = 2500 \text{ kg/m}^3$ for this study.

2. PV CELL MODELING

The end result of the manufacturing processing steps described in Section 1.2 is the complete PV cell is shown in Fig. 4. In addition to the basic device architecture, this figure illustrates three of the most important optoelec-

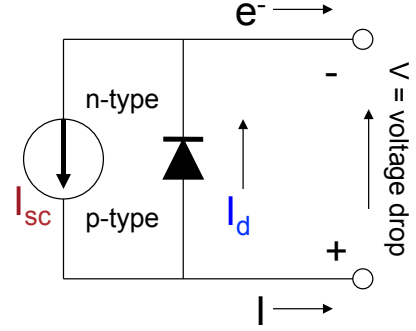


Fig. 5. The equivalent circuit model, where I denotes conventional current (not electron current).

tronic phenomena at work: the photon interactions that generate electron/hole pairs, how the charge carriers are swept through the pn -junction, and how recombination of the charge carriers reduces the net electrical current produced by the PV cell.

When the two electrodes of Fig. 4 are connected by a *short circuit*, there is no applied (external) voltage drop V and the diffusion and drift currents corresponding to the thermally-generated electron-hole pairs balance each other across the junction, resulting in zero diode current $I_d = 0$. In this situation, the maximum external current flows and is denoted I_{sc} . No external current flows under *open circuit* conditions and so all current flows within the PV cell resulting in $I_{sc} = I_d$; this gives rise to the maximum voltage drop between the contacts V_{oc} .

The limiting conditions described above and the I vs. V characteristics in between can be illustrated by the equivalent circuit model shown in Fig. 5. The modeling equation for the complete circuit now is

$$I = I_{sc} + I_o \left[1 - \exp\left(\frac{qV}{k\beta T}\right) \right] \quad (3)$$

with the conventional short circuit $I_{sc} \geq 0$ and dark saturation $I_o \geq 0$ currents. In the circuit model, β is the diode ideality factor; $\beta \rightarrow 1$ if recombination takes place primarily in the quasi-neutral regions of the cell, and $\beta \rightarrow 2$ if in the depletion region. Gray (2003) states that recombination in each region typically is comparable, and so we chose $\beta = 1.5$ for a nominal value. Two-diode as well as models that take into account series and shunt resistance effects can be found in Gray (2003) and Ishaque et al. (2011); these and other model elements will be addressed in follow-up studies to this paper.

Following Gray (2003), a concept central to modeling PV cell performance is to factor I_{sc} in (3) in the following manner

$$I_{sc} = \eta_c^{int} I_{gen}$$

where η_c^{int} is the *internal collection efficiency* of the cell and I_{gen} the light-generated current. The former depends solely on charge-carrier recombination within the cell and approaches unity as carrier lifetime approaches infinity and surface recombination velocities approach zero. With this information, we can conceptually split the modeling tasks into two components, where

- (1) the optical modeling effects appear only in the term I_{gen}

(2) surface and bulk recombination rates will affect both η_c^{int} and I_o .

We begin by developing a model for I_{gen} , the *solar/optical model*.

3. SOLAR/OPTICAL MODEL

To compute the light-generated current/area (A/m^2)

$$I_{gen} = \frac{(1-s)q}{E_{bg,2}} \int_{\lambda_a(x)}^{\lambda_g(x)} [1-r(w,x,\lambda)] E_{sep}(\lambda) SR^* d\lambda \quad (4)$$

where $q = 1.6022 \times 10^{-19}$ C is the elementary charge and s is the fraction of the cell surface covered by electrodes (typically $s = 0.1$). If we denote $E_{sep,u}$ to be the usable fraction of the AM1.5 solar spectral power density function (spectral irradiance, see Fig. 6)¹, we define the spectral responsivity $SR^*(\lambda)$ by

$$E_{sep,u}(\lambda) = E_{sep}(\lambda) \frac{E_{bg,2}}{hc/\lambda} = E_{sep}(\lambda) SR^*(\lambda) \quad (5)$$

where $E_{bg,2} = 1.12$ eV the band gap of Si, $c = 2.9979 \times 10^8$ m/s is the speed of light, and $h = 4.1357 \times 10^{-15}$ eV·s is Planck's constant. The Si band gap of $E_{bg} = 1.12$ eV means that only light of wavelength $\lambda < 1107$ nm can generate electron/hole pairs, therefore, all longer wavelength radiation (see Fig. 6) passes through the PV cell or is absorbed, but only to heat the PV cell in the latter case.

3.1 Absorbance

Light absorption in thin films generally is modeled as an exponential function of film thickness with a wavelength-dependent absorption coefficient. Effective AR films should be mostly transparent, except for those wavelengths that fall below the critical value defined by the material band gap. Therefore, we will model absorption as a high-frequency filter, with the cut-off wavelength λ_a defined by the compositionally-dependent band gap (2):

$$\lambda_a(x) = \frac{hc}{E_{bg,1}(x)}.$$

The effect of AR film absorption is included in the solar/optical model as the lower limit of integration in (4).

3.2 Reflectance

Given a film thickness w , a range of wavelength λ , and n_0 , n_1 , and n_2 as the refractive indices of the surrounding medium, AR film, and Si, respectively (see Fig. 4), for a single-layer AR film at normal incidence the equations for the s - and p -polarization components become equal in magnitude and can be written as the single-interface reflectance terms

$$r_{01} = \frac{n_1 - n_0}{n_1 + n_0}$$

$$r_{12} = \frac{n_2 - n_1}{n_2 + n_1}$$

¹ The spectrum of sunlight reaching the Earth's surface after passing through the equivalent of 1.5 atmospheres, typically written with units $W/(m^2nm)$.

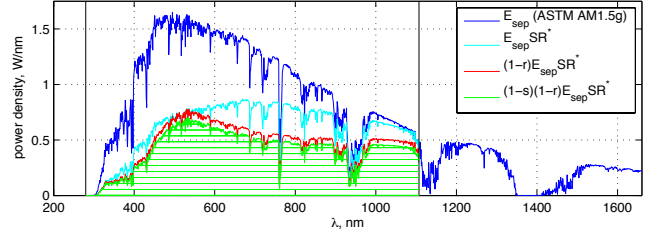


Fig. 6. *AM1.5, normalized to 1 kW/m². Integrated green curve translates to maximum current that can be generated with 100% quantum efficiency.*

The first and second-surface reflected wave phase difference

$$\phi_d = \frac{2\pi}{\lambda} n_1 w$$

results in maximum destructive interference when the film thickness w corresponds to $\lambda = 4n_1(x)w$ (see Kishore et al. (1997) for a brief introduction and Melles Griot (2009) for more details). The final form of the total reflectance is given by

$$r(w,x,\lambda) = \frac{r_{01}^2 + r_{12}^2 + 2r_{01}r_{12} \cos 2\phi_d}{1 + r_{01}^2 r_{12}^2 + 2r_{01}r_{12} \cos 2\phi_d}.$$

We note that this relationship remains valid in the limit of $w \rightarrow 0$. For this study, we take $n_0 = 1$ corresponding to air and an Si refractive index $n_2 = 3.85$ from Winderbaum et al. (1997). As described earlier, the film index of refraction n_1 is composition-dependent and given by equation (1).

3.3 Light-generated current I_{gen}

At this point, all of the model elements for the solar/optical module are in place to compute I_{gen} . A representative result is shown in Fig. 6 corresponding to $x = 1$ and $w = 200$ nm, a poorly-designed AR film that has minimum reflectances at $\lambda = 310$ and 520 nm and results in $I_{gen} = 260$ W/m².

4. DEVICE MODEL

Modeling the relationship between AR film properties and the diode model parameters η_c^{int} and I_o is the most challenging and poorly understood aspect of the PV cell simulation elements we consider. In the analysis that follows, we will set the internal collection efficiency to a constant value $\eta_c^{int} = 1$ and limit our focus to determining the dark saturation current density I_0 dependence on AR layer composition x .

Gray (2003) states I_o is inversely proportional to minority-carrier diffusion length, which itself is proportional to the square root of carrier lifetime τ_n under the long-base approximation. This gives

$$I_o = f \left(\frac{1}{\sqrt{\tau_n}} \right). \quad (6)$$

Data provided in Lelievre et al. (2009) provide a strong indication that measured τ_n are proportional to $1/x$; data in Soppe et al. (2005) indicate a linear correlation between n_1 and τ_n (see equation 1) further supporting this

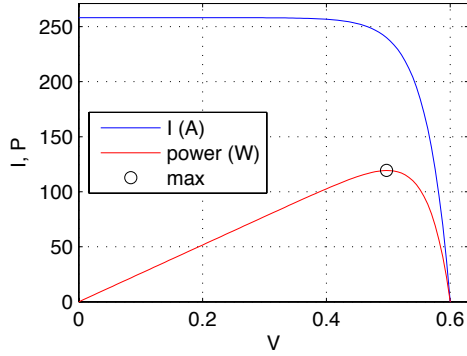


Fig. 7. I versus V and power versus V characteristics for the nominal PV cell (no AR film). The maximum power is 119 W and so corresponds to $\eta = 11.9\%$.

relationship. Therefore, we fit the data of Lelievre et al. (2009) to the following function

$$\tau_n(x) = \frac{800}{x + 0.1} - 500 \mu\text{s} \quad (7)$$

a relationship that is physically reasonable over the range $x \in [0, 1.4]$, covering the entire potential range of surface composition.

Our base (uncoated) PV cell design is modeled after Gray (2003) (see Table 3.2 and Fig. 3.16 of the cited work) and corresponds to $V_{oc} = 0.6$ V and $I_{sc} = 260$ A/m². Fitting these values to the diode equation (3) and using (7) in (6) we find

$$I_o(x, w) = 5.78 \times 10^{-5} \left[H(w) \sqrt{\frac{350}{\tau_n(x)}} + 1 - H(w) \right] \text{ A/m}^2 \quad (8)$$

where $H(w)$ is the Heaviside function, used to make the relationship (8) valid for $w = 0$. The I versus V and device power versus V plots for the nominal PV cell design is shown in Fig. 7.

4.1 Optimal cell efficiency

Defining the solar cell efficiency

$$\eta = \frac{P_{mp}}{1 \text{ kW/m}^2}$$

we examine η as a function of x and thickness w and plot the result in Fig. 8. Two important conclusions can be drawn from this map: the first is that the AR/passivation film can have a dramatic effect on the cell performance. In our system, the addition of the film improved cell efficiency from 11.9 to 17%. The second conclusion is that the efficiency map is a relatively complicated function of both film composition and thickness – in fact, we observe more than one local maximum for efficiency. However, the behavior demonstrated makes physical sense: smaller values of x improve carrier lifetime, but this is counteracted by the increasing index of refraction of the film. Likewise, a minimal film thickness of slightly less than 100 nm is needed to correspond to the 1/4 wave maximum interference criterion, resulting in the optimal value of $w = 75$ nm.

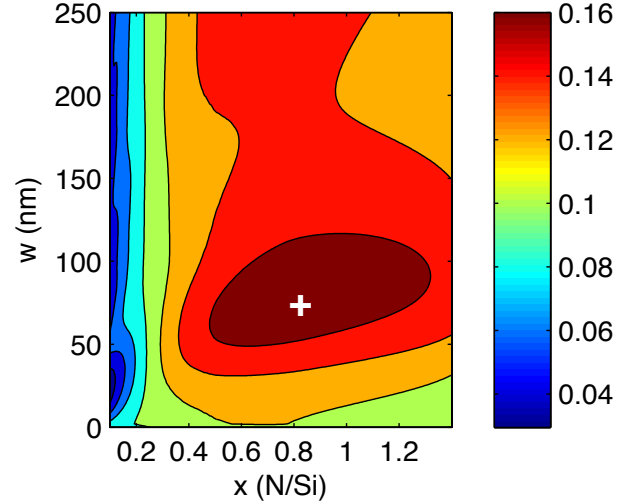


Fig. 8. PV cell efficiency as a function of AR film composition x and thickness w . The maximum cell efficiency is $\eta = 17\%$ found for $x = 0.77$ and $w = 75$ nm and is marked by the + symbol.

5. PECVD REACTOR SYSTEMS

PECVD reactor systems can be broadly split into direct and remote systems, although some designs can be operated in either mode depending on plasma power level (e.g., Hanyaloglu and Aydil (1998)). In direct PECVD, the substrate is in direct contact with the plasma; these systems generally feed both the NH_3 (and/or N_2) and SiH_4 through a porous shower head that also serves as the upper electrode. Direct plasma systems include large-area substrate systems such as the reactor described in Sansonnens et al. (2003).

In remote PECVD (RPECVD), the substrate is physically removed from the plasma region; furthermore, this allows separate injection of the nitrogen-containing precursor into the plasma to form nitrogen radical species. The separate SiH_4 sources are placed more closely to the growth surface, such as the design described by Soppe et al. (2005). The intended effect of this design is to reduce the formation of high molecular weight gas-phase Si-N compounds and to expose the growth surface to only the electrically neutral radicals and not the charged species themselves. The configuration of the system created for this study is shown in Fig. 9.

The major process manipulated variables are reactor total pressure P , plasma power level p_W , NH_3 and SiH_4 flow rates (q_N and q_S , respectively), and substrate temperature T . These operational parameters affect the reactor process characteristics, such as precursor utilization rates and total deposition time, as well as film characteristics such as spatial uniformity, film chemical composition, and growth rate. Typical process operating conditions are substrate temperature $T = 300$ to 400° C, deposition time $\tau \approx 2$ min, and total pressure P on the order of 100-500 mTorr.

5.1 PECVD process modeling

We split the reactor into two regions: the upper, remote plasma and the lower deposition chamber regions, a de-

species	NH ₃	NH ₂	H ₂	SiH ₄	SiH ₃	SiH ₂	SiH ₂ NH ₂
number i	1	2	3	4	5	6	7
mol mass M_i^w	17.03	16.02	2.02	32.12	31.11	30.10	46.12

Table 1. Reaction species present in the plasma and deposition chambers.

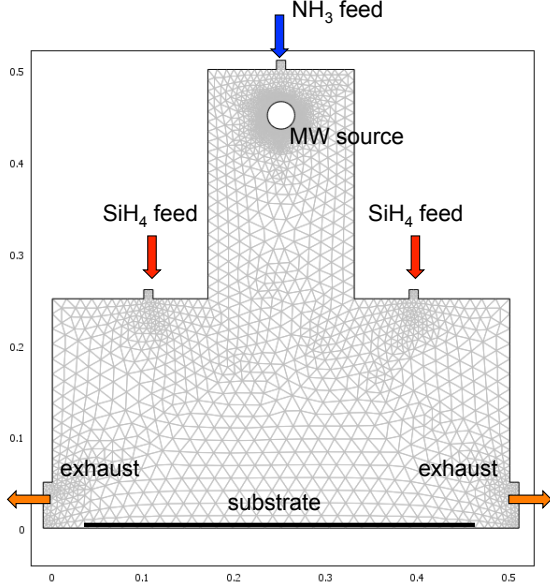


Fig. 9. PECVD reactor geometry and FE mesh used in subsequent calculations. Dimensions shown are in (m).

sign approximating the RPECVD systems of Kushner (1992) and Soppe et al. (2005). The Si and N precursors, the decomposition products, and the gas-phase deposition species considered in this work are listed in Table 1. To develop some sense for the relative magnitudes of convective and diffusive transport of the gas-phase constituents, we use the COMSOL finite-element simulation package to perform a simulation to examine the spatial distribution of NH₃ and SiH₄ under nominal, but unreactive, operating conditions.

The results of this simulation are seen in Fig. 10 where we observe the flow field streamlines and the concentration profile corresponding to SiH₄ (NH₃ makes up the other binary component). The gas flow is laminar under these operating conditions and it is clear that normal diffusion of the gas-phase species practically eliminates spatial gradients in the lower, deposition chamber. While there is significant back-diffusion of SiH₄ up to the plasma chamber, NH₃ is the primary component in this part of the reactor. Because of the insignificant across-wafer compositional gradients and because of the composition separation that exists between the chambers, for our initial study we will treat each section as a separate, perfectly mixed reactor region and will only consider the one-way transport of N-containing compounds from the plasma to the deposition chamber for this phase of the study.

5.2 Reaction mechanisms - remote plasma region

Nitrogen-containing radicals are generated in the plasma through interactions with the plasma electrons. Because of the geometry of the remote plasma source, the SiH₄

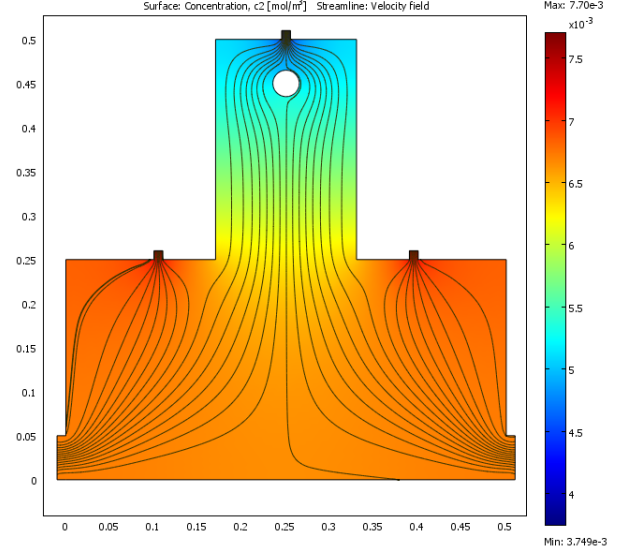


Fig. 10. PECVD reactor flow field streamlines, and SiH₄ concentration profiles for the isothermal PECVD reactor system operating at the nominal process operating conditions.

injected into the deposition chamber is not directly dissociated by the plasma. We note that in our modeling assumptions, ions are omitted because of their low concentration relative to the electrically neutral radicals. As shown in equation (7) of Masi et al. (1994), electron concentration is directly proportional to plasma power p_W and so the rate expression corresponding to reaction (g1) can be written as

$$r_1^g = n_e k_1' c_1 = (3.9s^{-1}) \frac{p_W}{p_W^o} c_1.$$

For the reaction rate term above, we adopt the rate constant $k_1' = 9 \times 10^{-16} \text{ m}^3/\text{s}$ and mean electron density $n_e = 4.3 \times 10^{15} \text{ m}^{-3}$ from Sansonnens et al. (2003) and will set the nominal plasma power to $p_W^o = 200 \text{ W}$.

Neutral species reactions - both regions For the remaining gas phase reactions, we consider a set of reactions and reaction rates (listed in Table 2) taken as a combination of those described in Sansonnens et al. (2003), Masi et al. (1994), and Kushner (1992). All of the reactions (g2-g6) apply to the deposition chamber, while only the radical formation and recombination reactions (g1-g2) are relevant to the remote plasma chamber.

We note the particular importance of reaction (g3): it is the only reaction in the list that can form a Si-containing radical from the feed SiH₄, a reaction which initiates the subsequent chain of reactions (g4-g6). While Kushner (1992) argues the NH₂ is relatively unreactive, the rate constant provided in that study (and listed in Table 2) shows that it actually is a dominant reaction in the gas phase, and so we include it in this study. The chemical species numbering system is contained in Table 1.

number	reaction	rate r_i^g , mol/(m ³ s)	Δn_i^g	ref
g1	$\text{NH}_3 + e^- \rightarrow \text{NH}_2 + 1/2\text{H}_2 + e^-$	*	0.5	a
g2	$\text{NH}_2 + 1/2\text{H}_2 \rightarrow \text{NH}_3$	$1.26 \times 10^6 \exp(-4277/T)c_2c_3$	-0.5	b
g3	$\text{SiH}_4 + \text{NH}_2 \rightarrow \text{SiH}_3 + \text{NH}_3$	$4.82 \times 10^4 c_4 c_2$	0	b
g4	$\text{SiH}_3 + \text{NH}_2 \rightarrow \text{SiH}_2\text{NH}_2 + 1/2 \text{H}_2$	$6.02 \times 10^7 c_5 c_2$	-0.5	b
g5	$2\text{SiH}_3 \rightarrow \text{SiH}_2 + \text{SiH}_4$	$1.51 \times 10^7 c_5^2$	0	c
g6	$\text{SiH}_2 + \text{NH}_2 \rightarrow \text{SiH}_2\text{NH}_2$	$3.01 \times 10^7 c_6 c_2$	-1	b

Table 2. Gas-phase reactions. T is in K and reference (a) corresponds to Sansonnens et al. (2003), (b) to Kushner (1992); (c) to Masi et al. (1994). For * see Section 5.2.

Simplification for the remote plasma region We consider material balance on the three species NH_3 , NH_2 , and H_2 in that order, neglecting surface reactions in the cold-wall plasma chamber. The two gas-phase reaction rates are defined as

$$r_1^g = k_1 \frac{p_W}{p_W^o} c_1, \quad r_2^g = k_2 c_2 c_3$$

and are used in the three species material balance and total molar flow balance equations as

$$\begin{aligned} V \frac{dc_1}{dt} &= -Vr_1^g + Vr_2^g + q^{in}c_1^{in} - q^{out}c_1 \\ V \frac{dc_2}{dt} &= Vr_1^g - Vr_2^g - q^{out}c_2 \\ V \frac{dc_3}{dt} &= \frac{1}{2}Vr_1^g - \frac{1}{2}Vr_2^g - q^{out}c_3 \\ 0 &= \frac{P}{R_g T} (q^{in} - q^{out}) + V (\Delta n_1^g r_1^g + \Delta n_2^g r_2^g) \end{aligned}$$

While the reactor dynamics become critical as the process is tuned to maximize precursor utilization, we will limit our study to steady-state deposition. The small set of nonlinear equations that result are easily solved using the Newton-Raphson method; we use the MATLAB-based modular simulation framework first described in Chen and Adomaitis (2006). Of particular interest at this stage in the modeling work is the relationship between the molar conversion rate ϕ_N of NH_3 to NH_2

$$\phi_N = \frac{q^{out}c_2}{q^{in}c_1^{in}}$$

to the total inlet flow rate of NH_3 (q_{in}), plasma power (p_W) and total chamber pressure (P). The results can be seen in Fig. 11 for three different values of total pressure P and a range of NH_3 feed flow rates and plasma power. Not surprisingly, the molar conversion of NH_3 to NH_2 is highest at low feed flows and high plasma power levels; the reaction to the radical species also is favored for higher pressures.

5.3 Surface reaction mechanisms

Again, we choose a relatively simplified set of surface reactions (Table 3), also patterned after Masi et al. (1994) where (s) indicates film species. It is interesting to see that with the exception of one case, no change in the number of gas-phase moles Δn_i^s occurs as a result of the surface reactions. We note that not all $N_s = 7$ species listed in Table 1 are involved in the surface reactions.

To compute the surface reaction rate r_j^s corresponding to $N_u = 5$ reactions (s1-s5), we use the kinetic theory of gases from which the flux of species j at the growth surface is

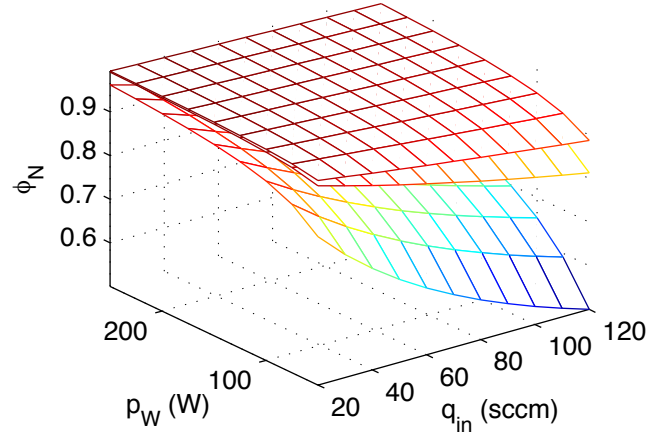


Fig. 11. Percentage conversion of NH_3 to NH_2 for $P_{tot} = 100$ mTorr (bottom surface), 500 mTorr (middle), and 1000 mTorr (top).

$$J_j = \frac{P_j}{\sqrt{2\pi M_j^w R_g T}} = c_j \sqrt{\frac{R_g T}{2\pi M_j^w}} \quad \left(\frac{\text{mol}}{\text{m}^2 \text{s}} \right)$$

where M_j^w , P_j , and c_j are the the molecular mass, partial pressure, and concentration of each precursor species j , respectively, and R_g is the gas constant.

Defining $w \in [0, w_t]$ as the spatial position within the film of total thickness w_t ($w = 0$ denotes the substrate/film interface and $w = w_t$ the growth surface) and z_i , $i = \text{N, S, or H}$ as the mole fraction of each element found in the film, we can write the film evolution model as

$$\begin{aligned} \frac{dw_t}{dt} &= \frac{1}{\rho} \sum_{i=1}^{N_u} M_i^{wd} r_i^s \\ z_N(w_t) &= \frac{r_1^s(z_N) + r_4^s}{r_{tot}^s(z_N)} \\ z_S(w_t) &= \frac{r_2^s + r_3^s + r_4^s + r_5^s}{r_{tot}^s(z_N)} \\ z_H(w_t) &= \frac{r_2^s - r_5^s(z_H)}{r_{tot}^s(z_N)} \end{aligned}$$

with

$$r_{tot}^s = r_1^s(z_N) + 2r_2^s + r_3^s + 2r_4^s + 2r_5^s.$$

5.4 Complete deposition chamber model

With the $N_r = 6$ reactions listed in Table 2, we can write the $(N_r \times 1)$ vector of reaction rates as \mathbf{r}^g and define an $(N_s \times N_r)$ array \mathbf{S} where each element $S_{i,j}$ corresponds to

number	reaction	rate r_j^s , mol/(m ² s)	sticking coeff f_i	Δn_i^g	M_i^{wd}
s1	NH ₂ → N(s) + H ₂	$f_1^s J_2(4/7 - z_N)$	1	0	15.01
s2	SiH ₃ → SiH(s) + H ₂	$f_2^s J_5$	1	0	29.09
s3	SiH ₂ → Si(s) + H ₂	$f_3^s J_6$	1	0	28.08
s4	SiH ₂ NH ₂ → SiN(s) + 2H ₂	$f_4^s J_7$	0.005	1	43.09
s5	SiH ₂ NH ₂ → SiH(s) + NH ₃	$f_5^s J_7$	0.005	0	29.09

Table 3. *Surface reactions and reaction rates.*

the number of species i produced (positive) or consumed (negative) by gas-phase reaction j . For our system

$$\mathbf{S} = \begin{bmatrix} -1 & 1 & 1 & 0 & 0 & 0 \\ 1 & -1 & -1 & -1 & 0 & -1 \\ 1/2 & -1/2 & 0 & 1/2 & 0 & 0 \\ 0 & 0 & -1 & 0 & 1 & 0 \\ 0 & 0 & 1 & -1 & -2 & 0 \\ 0 & 0 & 0 & 0 & 1 & -1 \\ 0 & 0 & 0 & 1 & 0 & 1 \end{bmatrix}.$$

Likewise, array $\mathbf{U}^{N_s \times N_u}$ relates the surface reaction rates to the gas phase material balances

$$\mathbf{U} = \begin{bmatrix} 0 & 0 & 0 & 0 & 1 \\ -1 & 0 & 0 & 0 & 0 \\ 1 & 1 & 1 & 2 & 0 \\ 0 & 0 & 0 & 0 & 0 \\ 0 & -1 & 0 & 0 & 0 \\ 0 & 0 & -1 & 0 & 0 \\ 0 & 0 & 0 & -1 & -1 \end{bmatrix}$$

and so that material balance and volumetric outflow equations can be written as

$$V \frac{dc_i}{dt} = q^{in} c_i^{in} - q^{out} c_i + V \mathbf{S} \mathbf{r}^s + A \mathbf{U} \mathbf{r}^s \quad (9)$$

$$0 = \frac{P}{R_g T} (q^{in} - q^{out}) + V \sum_{j=1}^{N_g} \Delta n_j^g r_j^g + A \sum_{j=1}^{N_u} \Delta n_j^s r_j^s \quad (10)$$

for $i = 1, \dots, N_g$.

5.5 Representative deposition rates and film compositions

Despite their relatively simple form, it can be challenging to compute steady-state solutions to (9)-(10) due to the sensitivity of the Newton-Raphson method's convergence behavior to initial solution estimates. Therefore, a predictor-corrector continuation technique was used to find solutions at selected sets of parameter values, or over a range of values as illustrated in Fig. 12, starting from limiting reactor conditions that allowed the computation of accurate initial solution estimates.

Two important observations can be made in Fig. 12. First, we see that a unique deposition rate maximum exists; this is due to the surface reactions shutting down as $q_S \rightarrow 0$ and the dilution of the surface reaction precursors as $q_S \rightarrow \infty$. Second, we observe two deposition regimes: as described in Kushner (1992), the “atomic” regime is found for smaller values of q_S where the deposition is due to significant rates of (s1-s3), and a “molecular” regime where the film forms primarily from the deposition of amino-silane complexes by surface reactions (s4-s5). Both the optimal silane flow corresponding to $x = 0.77$ and the maximum deposition rate fall midway between the two regimes.

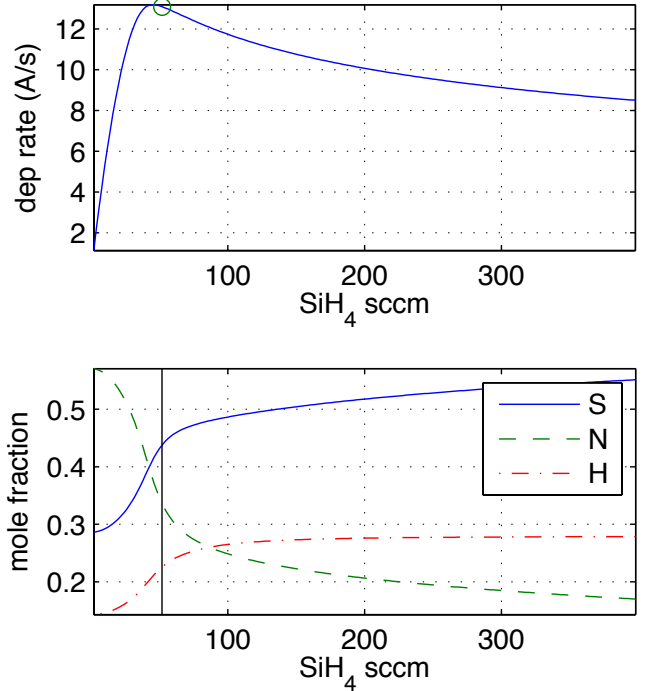


Fig. 12. *Deposition rate (top) and film composition as a function of SiH₄ inlet flow.*

5.6 Process optimization

In Fig. 12, we observe that the values of q_S (SiH₄ sccm) corresponding to the optimal film composition $x = 0.77$ and maximum deposition rate nearly coincide. This is good, but it is likely we can adjust P , T , p_W , and q_N such that higher deposition rates result for the same value of x . Preliminary numerical results indicate this is true - for example, the deposition rate is found to increase with total chamber pressure P . A more systematic study is underway.

An interesting observation is that the optimal value of q_S is *reduced* for higher values of P - keep in mind that the deposition rate *also increases* over the base case under these conditions. This observation opens the door to developing more sophisticated process optimization, where manufacturing efficiency metrics such as total tool throughput and precursor utilization can simultaneously be optimized. Again, this is the subject of current investigation.

6. CONCLUSIONS

The objective of this study was to demonstrate that a complete, physically based model can be developed that describes the role manufacturing process inputs have on the ultimate efficiency of crystalline Si solar cells. The scope of

the modeling work was limited to the anti-reflection film PECVD manufacturing step; follow-up research will focus on developing models for the phosphorous doping, surface texturizing, and final firing steps of the complete manufacturing process. Likewise, much room for improvement exists in terms of process optimization – for example, it is possible to adjust P , T , p_W , and q_N such that higher deposition rates result for the same value of film composition x . Mapping out these regimes of higher deposition rates currently is under study.

Finally, our modeling opens the door to developing more sophisticated process optimization approaches (e.g., dynamic optimization), where manufacturing efficiency metrics such as tool throughput and precursor utilization can simultaneously be optimized with PV product efficiency η . The full potential of our modeling approach will be realized when both the manufacturing and product performance measures are optimized in this manner.

REFERENCES

- Alvarez, F. and A. A. Valladares, The atomic and electronic structure of amorphous silicon nitride *Revista Mexicana de Fisica* **48** 528-533 (2002).
- Breyer, Ch., Ch. Birkner, F. Kersten, A. Gerlach, G. Stryi-Hipp, J. Ch. Goldschmidt, D. F. Montoro, and M. Riede, Research and development investments in PV – A limiting factor for a fast PV diffusion? *25th EU PVSEC / WCPEC-5*, Valencia, Spain (2010).
- Ceccaroli, B. and O. Lohne, Chapter 5: Solar grade silicon feedstock, In *Handbook of Photovoltaic Science and Engineering*, A. Luque and S. Hegedus (Ed.), John Wiley & Sons, Ltd (2003).
- Chen, J. and R. A. Adomaitis, An object-oriented framework for modular chemical process simulation with semiconductor processing applications *Computers & Chem. Eng* **30** 1354-1380 (2006).
- Dollet, A., L. Layeillon, J. P. Couderc, and B. Despax, Analysis and modelling of a pulsed-plasma reactor for silicon nitride deposition: reactor optimization *Plasma Sources Sci. Technol.* **4** 459-473 (1995).
- Gay, C. Applied Materials, Inc., private communication (2011).
- Gray, J. I. Chapter 3: The physics of the solar cell, In *Handbook of Photovoltaic Science and Engineering*, A. Luque and S. Hegedus (Ed.), John Wiley & Sons, Ltd (2003).
- Hanyaloglu, B. F. and E. S. Aydil, Low temperature plasma deposition of silicon nitride from silane and nitrogen plasmas *J. Vac. Sci. Technol. A* **16** 2794-2803 (1998).
- Ishaque, K., Z. Salam, and H. Taheri, Simple, fast and accurate two-diode model for photovoltaic modules *Solar Energy Mater. & Solar Cells* **95** 586594 (2011) .
- King, S. W., Plasma enhanced atomic layer deposition of $\text{SiN}_x\text{:H}$ and SiO_2 *J. Vac. Sci. Technol. A* **29** (2011)
- Kishore, R. A. M., S. N. Singh, and B. K. Das Screen printed titanium oxide and PECVD silicon nitride as antireflection coating on silicon solar cells *Renewable Energy* **12** 131-135 (1997).
- Kushner, M. J., A model for the discharge kinetics and plasma chemistry during plasma enhanced chemical vapor deposition of amorphous silicon *J. Appl. Phys.* **63** 2532-2551 041501-1-9 (1988).
- Kushner, M. J., Simulation of the gas-phase processes in remote-plasma-activated chemical-vapor deposition of silicon dielectrics using rare gas-silane-ammonia mixtures *J. Appl. Phys.* **71** 4173-4189 (1992).
- Lelievre, J.-F., E. Fourmond, A. Kaminski, O. Palais, D. Ballutaud, and M. Lemiti Study of the composition of hydrogenated silicon nitride $\text{SiN}_x\text{:H}$ for efficient surface and bulk passivation of silicon *Solar Energy Mat. & Solar Cells* **93** 1281-1289 (2009).
- Masi, M., G. Besana, L. Canzi, and S. Carra, Modeling of silicon nitride deposition by RF plasma-enhanced chemical vapor deposition *Chem. Engng Sci.* **49** 669-679 (1994).
- Melles Griot, *Technical Guide*, Vol. 2, Ch 5 (2009).
- Ranjan, S., S. Balaji, R. A. Panella, and B. E. Ydstie, Silicon solar cell production, *Comp. & Chem. Engng* **35** 14391453 (2011) .
- Sansonnens, L., J. Bondkowski, S. Mousel, J.P.M. Schmitt, and V. Cassagne, Development of a numerical simulation tool to study uniformity of large area PECVD film processing *Thin Solid Films* **427** 21-26 (2003).
- Soppe, W., H. Rieffe, and A. Weeber, Bulk and surface passivation of silicon solar cells accomplished by silicon nitride deposited on industrial scale by microwave PECVD *Prog. Photovolt: Res. Appl.* **13** 551-569 (2005).
- Wenhan, S. R., M. A. Green, M. E. Watt, and R. Corkish, *Applied Photovoltaics*, 2nd ed. Earthscan (2007).
- Winderbaum, S., F. Yun, and O. Reinhold, Application of plasma enhanced chemical vapor deposition silicon nitride as a double layer antireflection coating and passivation layer for polysilicon solar cells *J. Vac. Sci. Technol. A* **15** 1020-1025 (1997).
- Zerga, A. M. Carrada, M. Amann, and A. Slaoui, Si-nanostructures formation in amorphous silicon nitride $\text{SiN}_x\text{:H}$ deposited by remote PECVD *Physica E* **38** 21-26 (2007).